Attosecond Ionization and Tunneling Delay Time Measurements in Helium

P. Eckle, *et al.*

Erratum: please note that in Eq. (2) the unit of Δt_T should be femtosecond (fs) and not attosecond (as).
All the numbers reported in the text are anyway consistent with the correct units

38. S. Trebst, U. Schollwöck, M. Troyer, P. Zoller, *Phys. Rev. Lett.* **96**, 250402 (2006).
39. We thank E. Demler for fruitful discussions; T. Rom, D. van Oosten, and S. Braun for help during the setup of the experiment; and the Leibniz Institute of Surface Modification (IOM Leipzig) for providing the phase masks used in phase-contrast imaging. We acknowledge funding by the Deutsche Forschungsgemeinschaft

Attosecond Ionization and Tunneling Delay Time Measurements in Helium

P. Eckle,[1] A. N. Pfeiffer,[1] C. Cirelli,[1] A. Staudte,[2] R. Dörner,[3] H. G. Muller,[4] M. Büttiker,[5] U. Keller[1]

It is well established that electrons can escape from atoms through tunneling under the influence of strong laser fields, but the timing of the process has been controversial and far too rapid to probe in detail. We used attosecond angular streaking to place an upper limit of 34 attoseconds and an intensity-averaged upper limit of 12 attoseconds on the tunneling delay time in strong field ionization of a helium atom. The ionization field derives from 5.5-femtosecond-long near-infrared laser pulses with peak intensities ranging from 2.3×10^{14} to 3.5×10^{14} watts per square centimeter (corresponding to a Keldysh parameter variation from 1.45 to 1.17, associated with the onset of efficient tunneling). The technique relies on establishing an absolute reference point in the laboratory frame by elliptical polarization of the laser pulse, from which field-induced momentum shifts of the emergent electron can be assigned to a temporal delay on the basis of the known oscillation of the field vector.

The tunneling process is one of the primary manifestations of quantum mechanics' departure from classical physics. However, the question of whether tunneling through an energetically forbidden region takes a finite time or is instantaneous has been subject to ongoing debate over the past 60 years (*1*). Recently, experimental investigations of atomic interactions with intense laser fields (*2*, *3*) have failed to offer a definitive answer, and many different theoretical predictions seem to contradict each other (*4–7*).

Ionization of an atom in a strong laser field allows for addressing this question of a possible tunneling time in an experimentally and conceptually well-defined manner. The strong-field ionization process can be split in two distinct steps: First, the bound electron tunnels through the potential wall created by the superposition of the atomic Coulomb potential and the laser field. After tunnel ionization, the electron is usually treated as a free electron with zero initial kinetic energy at the exit of the tunnel. In the second step, the now-free electron is accelerated by the laser field and receives a linear drift momentum that only depends on the laser field strength at the time of tunneling. This is in strong analogy to the three-step model in high harmonic generation (*8*) using linearly polarized light.

In our experiment, we used close-to-circular polarization, thereby ensuring a unique relationship between the time at which the electron exits the tunnel and the direction of its momentum after the laser pulse. The measured momentum vector of the electron hence serves as the hand of a clock, indicating the time when the electron appeared from the tunnel in the laser field. The clock face is determined by the rotating electric field of the close-to-circularly polarized laser pulse. Thus, if we know the direction of laser field at time zero, $t_{0,\text{field}}$, when the tunneling process is initiated, we can determine the time the electron has spent in the tunnel in the classically forbidden region inside the potential wall. This difference or delay we refer to as the tunneling delay time, Δt_{D}.

The high-field ionization process exhibits different regimes that are distinguished by the Keldysh parameter, γ, which is given for circularly polarized light by (*9*)

$$\gamma = \frac{\omega_0 \sqrt{2 I_{\text{p}}}}{E_0} \text{ (atomic units)} \cong$$
$$0.327 \sqrt{\frac{I_{\text{p}}(\text{eV})}{I_0(10^{14}\text{W/cm}^2)[\lambda(\mu\text{m})]^2}} \quad (1)$$

where I_{p} is the ionization potential, ω_0 the center laser angular frequency, E_0 the electric field amplitude of the intense infrared (IR) laser pulse, I_0 the peak intensity of the pulse, and λ the laser wavelength. For example, for the helium ionization potential of 24.59 eV, a peak intensity of 10^{14} W/cm^2, and a center wavelength of 725 nm, we obtain $\gamma = 2.24$ for circular polarization (Eq. 1). For the same peak intensity, γ is a factor of $\sqrt{2}$ larger for circularly polarized light than for linearly polarized light. For $\gamma \gg 1$, that is, for short wavelength and low intensity, the ionization is most properly described by the simultaneous absorption of many discrete photons. On the other hand, if $\gamma \ll 1$, tunneling of the bound electron through a classical potential barrier provides the appropriate physical picture of the ionization process. The two regimes are not expected to be separated by a sharp transition, and both tunneling and multiphoton ionization contribute in the intermediate regime with $\gamma \approx 1$. Recently this intermediate regime was referred to as the regime of nonadiabatic tunneling (*12*). So far, all high laser field experiments have confirmed that, in this intermediate regime, the tunnel ionization is the dominant process, fully explaining, for example, high harmonic generation (*8*), quantum path interferences (*10*), and laser-induced electron tunneling and diffraction (*11*). A simple tunneling time was introduced by Keldysh (*9*) and more recently extended to the nonadiabatic tunneling regime (*12*), which formally agrees with the Büttiker-Landauer traversal time for tunneling, Δt_{T} (*9*, *13*):

$$\gamma = \omega_0 \Delta t_{\text{T}} \Rightarrow \Delta t_{\text{T}}(\text{as}) = 0.531 \cdot \gamma \cdot \lambda(\mu\text{m})$$
$$= 0.174 \times \sqrt{\frac{I_{\text{p}}(\text{eV})}{I_0(10^{14}\text{W/cm}^2)}} \quad (2)$$

We have experimentally explored the nonadiabatic tunneling regime in helium atoms exposed to laser fields with γ ranging from 1.45 to 1.17 corresponding to a peak intensity ranging from 2.3×10^{14} to 3.5×10^{14} W/cm^2 (Eq. 1), which in turn corresponds to a Δt_{T} between 450 to 560 as. At these intensities, over-the-barrier ionization (*14*) is negligible because for helium the critical intensity is $\approx 1 \times 10^{15}$ W/cm^2 (i.e., $\gamma = 0.71$ for circular polarization and $\lambda = 725$ nm).

Close-to-circularly polarized pulses with a duration in the two optical cycle regime (5.5 fs) and a center wavelength of 725 nm, which were produced by a Ti:Sapphire based laser system and a two-stage filament compressor (*15*), were focused onto helium atoms inside a COLTRIMS apparatus (*16*). Instead of measuring the electron momentum distributions directly, we recorded helium ion distributions. Momentum conservation

[1]Physics Department, Eidgenössische Technische Hochschule (ETH) Zürich, CH-8093 Zürich, Switzerland. [2]Steacie Institute for Molecular Sciences, National Research Council of Canada, 100 Sussex Drive, Ottawa, Ontario K1A 0R6, Canada. [3]Institut für Kernphysik, Johann Wolfgang Goethe Universität, Max-von-Laue-Straße 1, 60438 Frankfurt am Main, Germany. [4]Stichting voor Fundamenteel Onderzoek der Materie–Institute for Atomic and Molecular Physics, Kruislaan 407, 1098 SJ Amsterdam, Netherlands. [5]Physics Department, University of Geneva, CH-1211 Geneva, Switzerland.

Fig. 1. Angular calibration. p_x and p_y are the ion momentum components integrated over p_z along the laser propagation direction for both linearly (**A**) and elliptically (**B**) polarized light measured with the COLTRIMS. For both polarizations we measured the optical transmission through a rotating polarizer (red data points): Adjusting the wave plate for linear polarization we measured a 100% modulation depth in the transmission signal. For elliptical polarization, this modulation depth is reduced and so determines the amount of ellipticity introduced by the rotated wave plate. In addition, we measured for both polarizations also the ion momentum distribution (blue data below) where the angle is now determined by the streaking angle θ in the x-y plane. Because there is no angular streaking for linearly polarized light we obtained a direct calibration between the rotating polarizer angle and the streaking angle, and we set the difference to zero, that is, $\Delta\theta_{linear} = 0°$. a.u. indicates atomic units.
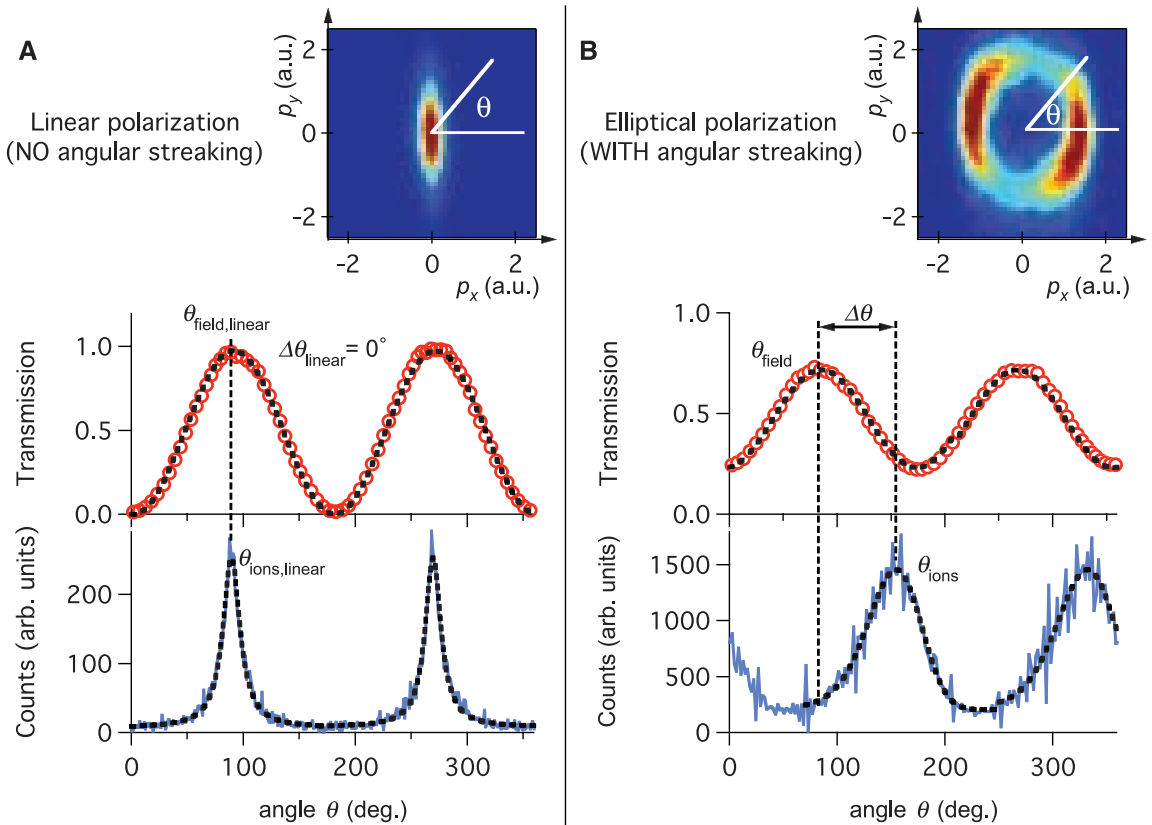
guarantees that the electron momentum is reflected in the parent ion. The explored Keldysh parameter range was limited in the current experimental setup at high intensities (i.e., small γ) by detector saturation and at low intensities (i.e., high γ) by acquisition time. In high laser field physics, this is a typical range of operation.

We discovered a technically very simple method for achieving absolute time zero calibration. By applying a close-to-circular and well-characterized ellipticity to the polarization of the pulse, we introduced small subcycle oscillations on the time-dependent electric field amplitude that became strongly enhanced in the angular ion momentum distribution (17). The main axis of the E-field ellipse provides a fixed reference point in time. The comparison of the major axis of the ellipse to the oscillations in the momentum distribution of the ionized helium atoms then directly yields the tunneling delay time Δt_D, as illustrated in Figs. 1 and 2. This method removes the need to stabilize or measure the laser pulse's carrier envelope offset phase (CEP) (18–20).

We used linearly polarized light to obtain an absolute angular reference that compares the angles extracted from the peak positions in the ion data with the angles obtained from the polarization measurement (Fig. 1A). In ionization by linearly polarized light, no angular streaking takes place; that is, the streaking angle offset has to be $\Delta\theta_{linear} = 0°$. Thus, field transmission and ion distribution are aligned in space independent of

any potential tunneling delay time. We measured the polarization direction with a polarizer and a power meter, obtaining a sinusoidal intensity modulation with a 100% contrast ratio (Fig. 1A, transmission through the polarizer versus polarizer angle). The angular direction, θ_{field}, of the polarization in the x-y plane is then determined by the maximum transmission and the maximum ion count measured in the COLTRIMS apparatus (Fig. 1A, counts versus angle).

The measurements with elliptically polarized pulses are shown in Fig. 1B. From the angle calibration obtained with linearly polarized light as described above, we know the angular orientation of the polarization ellipse in the x-y plane. Because the polarization measurement temporally integrates over the entire pulse field, it is independent of the CEP. In addition, the measured modulation contrast (Fig. 1B, transmission versus angle) determines the ellipticity of the incident pulse. In contrast to ionization under linear polarization, an electron that tunnels in a close-to-circularly polarized field will receive a drift momentum that points about 90° ahead of the laser field direction at the time of the exit of the tunnel, $t_{0,ion}$. Hence, the peaks in the observed ion momentum distribution resulting from the ellipticity are rotated about 90° from their angle at $t_{0,ion}$ (i.e., at the instant of ionization). This rotation of the streaking angle depends on the ellipticity and can be calculated with a semi-classical simulation (17, 21). Δt_D results from the angular

offset between the maximum of the electric field, $t_{0,field}$, which is given by the orientation of the polarization ellipse and the instant of ionization, $t_{0,ion}$, that is, $\Delta t_D = t_{0,ion} - t_{0,field}$. Such a tunneling delay time is then determined from the difference between the measured streaking angle, $\Delta\theta$ (Fig. 1B), and the calculated streaking angle assuming instantaneous tunneling.

With the help of Fig. 2, we explain why we can perform the tunneling delay time measurements without CEP stabilization. Figure 2A shows the measured two-dimensional He$^+$ ion momentum distributions and the corresponding one-dimensional radially integrated angular momentum distributions for four different CEP values. The two peaks change in relative intensity but are only weakly shifted in angle with changing CEP because the spatial orientation of the electric field ellipse (in red) is not CEP-dependent (17). The CEP vector (black) is rotating over a full cycle of 360°, whereas the direction of the maximum electric field vector (red) is defined by the ellipse and covers a much smaller angular span. Therefore CEP-dependent angular shifts become negligible, and the double peak ion structure is very well resolved even without CEP stabilization, as shown in Fig. 2B. This means that even without CEP stabilization the double peak oscillations do not smear out in space, which enables CEP-independent measurements.

The measured streaking angle, $\Delta\theta$, as a function of ellipticity is shown in Fig. 3. The elliptic-

Fig. 2. Determination of time zero using an elliptically polarized intense streaking field. No CEP stabilization is needed. (**A**) The polarization ellipse (red) and four helium momentum distributions in the polarization plane and the corresponding radially integrated distributions are shown for four different carrier envelope offset phases (CEPs). Whereas the CEP vector rotates over a full 360° cycle (black circle), the maximum electric field is moving only along a smaller angular span (red solid line) defined by the ellipse. The resulting ion distributions show the characteristic two peaks, whose angular position is only weakly changed upon a variation of the CEP. When the CEP vector points in the direction of the minor axis of the polarization ellipse (as sketched in the figure), the two peaks have similar intensity. A dominant peak in the ion distribution is obtained when the CEP vector points in the direction of the major axis of the ellipse. (**B**) The momentum distributions are accumulated over all CEP values in the calculation as well as in the data. The ellipticity peaks are clearly resolved also in the CEP-averaged case and can be used to determine $t_{0,ion}$.
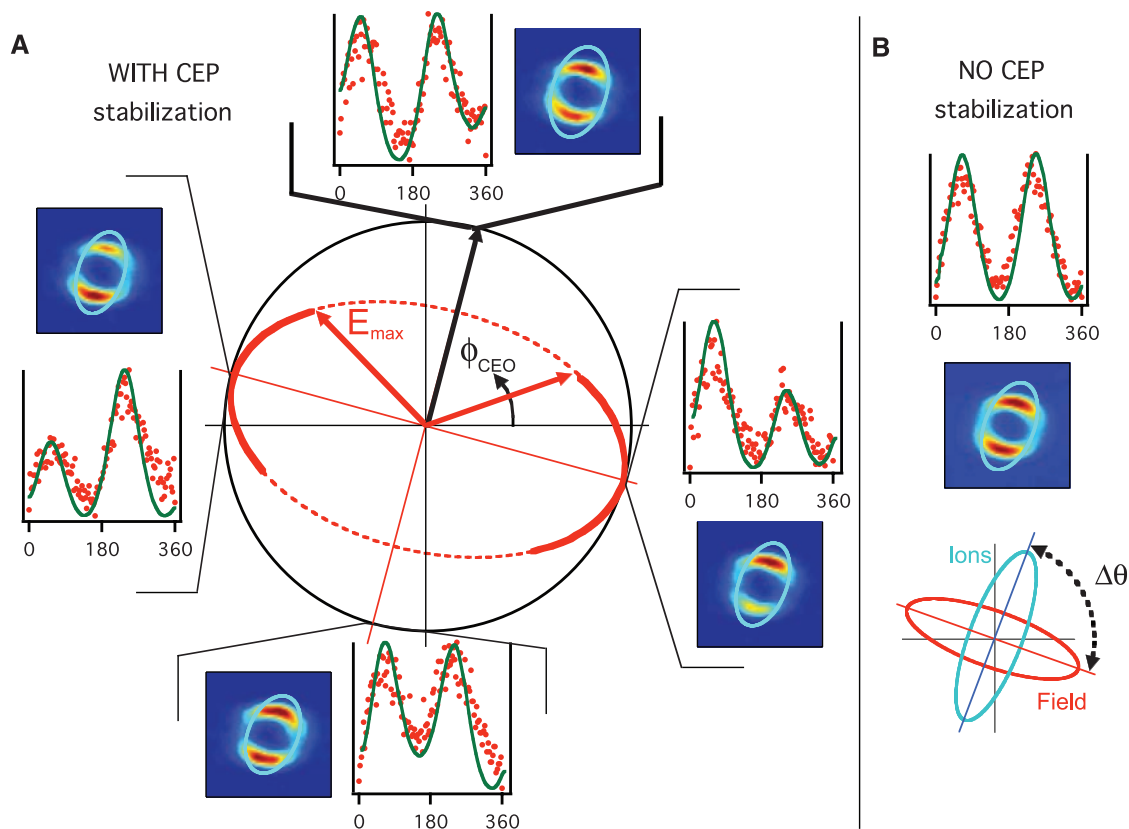
ity was adjusted by rotating a broadband quarter wave plate, which tunes the polarization between linear and circular extremes. The measured contrast ratio as described in Fig. 1 then gives a calibration between the wave plate angle and the ellipticity of the pulse. $\Delta\theta$ is shown for a constant intensity of 2.3×10^{14} W/cm^2, where the error bars result from the individual errors in the curve-fitting procedures for the polarization and helium ion momentum data (*21*). The error is highest for polarizations closer to circular because the peak-to-peak modulation decreases in the ion data as well as in the polarization measurement. These measurements are compared with a very simple semi-classical simulation without (dashed line in Fig. 3) and with (solid line in Fig. 3) Coulomb correction in the streaking assuming instantaneous tunneling. Therefore, $\Delta\theta$ gives access to Δt_D once the simulated zero-time-delay streaking angle is subtracted.

The simple semi-classical simulation (Fig. 3 dashed line) has its basis in the ADK (Ammosov, Delone, and Krainov) ionization rates, assuming instantaneous tunneling (*21, 22*) and classical propagation in the measured electric field of the pulse. We calculated angular momentum distributions averaged over all CEP values and obtained very good agreement with our measurements. This semi-classical simulation shows an average deviation of ≈6.5° with respect to the data. However, in this simulation we neglected the effect of the Coulomb potential between the electron and the

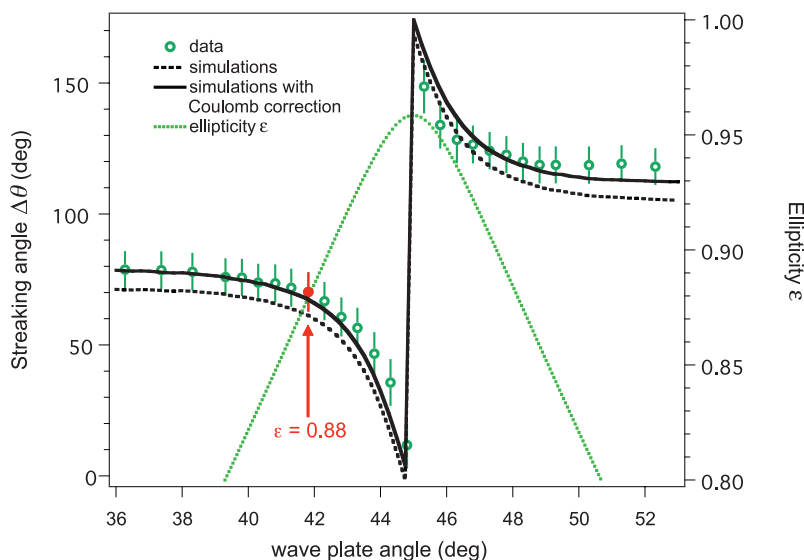**Fig. 3.** Measured streaking angle (data points) as a function of λ/4-wave plate angle (i.e., ellipticity) for a fixed peak intensity of ≈2.3 × 10^{14} W/cm^2. The semi-classical simulation assuming instantaneous tunneling with Coulomb correction in the streaking (solid line) gives a very good agreement with the measurement. In red, marked with an arrow, the value of ellipticity (0.88) at which the intensity dependent curve of Fig. 4 was measured.

parent ion during the streaking process. This Coulomb potential was incorporated into an additional simulation as a function of ellipticity varying from 0.7 to 1.00 at a fixed peak intensity of 2.3 × 10^{14} W/cm^2. The Coulomb potential was found to account for an additional 8.6° at an ellipticity of 0.7 to 5.5° at an ellipticity of 1.0 in the streaking angle, shifting the theoretical curve upward to higher angles (solid line in Fig. 3) as compared with the dashed curve in Fig. 3.

To determine the intensity dependence of a possible Δt_D, we then fixed the ellipticity to 0.88 (marked in red in Fig. 3) and varied the peak intensity from 2.3 to 3.5×10^{14} W/cm^2 (corresponding to a γ variation of 1.45 to 1.17, Eq. 1). The Coulomb correction in the streaking angle for an ellipticity of 0.88 gives 6.46° at 2.3×10^{14} W/cm^2 and 6.54° at 3.5×10^{14} W/cm^2. Thus, the Coulomb correction shows no significant intensity dependence of the streaking angle over the intensity range of our experiment. Figure 4 shows the measured Δt_D (data points) as a function of peak intensity and Keldysh parameter. This tunneling time delay is the difference between the measured streaking angle and the calculated propagation streaking angle, taking into account the 6.5° offset resulting from the Coulomb potential (solid line set to zero in Fig. 4). We measure a weighted intensity-averaged offset of 6.0 as with a standard deviation of 5.6 as, taking into account the individual data errors ranging between 14 and 20 as (21). This results in an intensity-averaged upper limit for the tunneling time delay of 12 as. The accuracy in this measurement is higher compared with the ellipticity-dependent streaking angle measurement presented in Fig. 3 for two reasons: First, at an ellipticity of 0.88, the modulation amplitudes in the ellipticity peaks for both the polarization measurement and the ion data are high enough to allow for more reliable peak fitting (Fig. 4); second, in this measurement, larger data sets were available because the measurement duration was extended. For a more conservative upper limit estimate of 34 as, we use the data point at the lowest intensity, which also has the largest de-

viation from zero and the largest error. At that intensity, the tunneling delay time was measured to be 13.9 as with an error of 19.7 (Fig. 4). We then obtain 34 as by adding 13.9 as and 19.7 as (21). Thus, we can conclude that we have measured a tunneling delay time with an upper limit of 34 as without any significant intensity dependence from 2.3×10^{14} to 3.5×10^{14} W/cm^2. In comparison, the traversal time for tunneling (Eq. 2) would vary between 450 to 560 as.

A numerical simulation based on the time-dependent Schrödinger equation of the ionization process reproduced the experimental observations: A few-optical-cycle pulse with close-to-circular polarization, with CEP chosen to simultaneously reach the maximum electric field strength of carrier and envelope at the center of the pulse, caused a single burst of ionization peaking in the direction 95° from that of the major polarization axis, with a full width at half maximum of 80° (21). Thus, the numerical simulations, like the experiment, lead to a momentum distribution that is consistent with a zero delay time for tunneling.

Among the numerous theoretical approaches toward addressing the tunneling time question, two principal frameworks are the Wigner-Eisenbud-Smith time delay (23) and the Buttiker-Landauer traversal time for tunneling (13). The Wigner-Eisenbud approach considers a wave packet and follows its peak. Such motion in the classically allowed region is characterized by the familiar group velocity. In the tunneling regime, the Wigner-Eisenbud time can be much shorter than the time necessary for propagation of light over the same distance and, if taken at face value, gives super-

luminal tunneling times. This concept is rather similar to superluminal group velocities discussed in the context of photon propagation through media with anomalous dispersion. Several objections are possible against the Wigner-Eisenbud approach: First, there is no conservation law in physics for peaks of wave packets; and, second, superluminal velocities cannot characterize a causal process. The answer of Sommerfeld and Brillouin to superluminal velocities in regions of anomalous dispersion was to characterize pulse propagation by a signal velocity, which is always limited by the velocity of light (24–26). The Buttiker-Landauer traversal time for tunneling is similarly an effort to obtain a more obviously physical answer for the speed of the tunneling process. In the Buttiker-Landauer approach, the height of the tunneling barrier is modulated in time, acting as a clock against which the tunneling time can be measured. This model leads to the distinction of an adiabatic regime, where the tunneling barrier oscillates slowly compared with the tunneling process, and a nonadiabatic regime, where the oscillation is fast. A traversal time for tunneling is obtained by considering the crossover between these two regimes. For linearly polarized light, the Buttiker-Landauer time is directly related to the adiabaticity parameter of Keldysh (9). In our experiment, a helium atom is ionized by an intense laser field, and we define a tunneling delay time, Δt_D, as the time delay between the lowering of the barrier and the time at which the escaping electron first experiences acceleration by the external field of the laser. This means that these two tunneling times consider entirely different aspects of the tunneling process.

Fig. 4. Measured tunneling time delay, Δt_D (data points), for a fixed ellipticity (i.e., ε = 0.88) as a function of peak intensity and Keldysh parameter (Eq. 1). The tunneling time delay is the difference between the measured and the calculated propagation streaking angle assuming instantaneous tunneling. In the calculated streaking angle, we also took into account the Coulomb potential (solid line set to zero). We measured an intensity-averaged offset of 6.0 as with a standard deviation of 5.6 as. The two-dimensional helium momentum distributions measured at different intensities and the corresponding radially integrated distributions spanning one optical cycle (2.44 fs) are shown on the right. The time axis was calibrated, and the calculated streaking time was deducted.
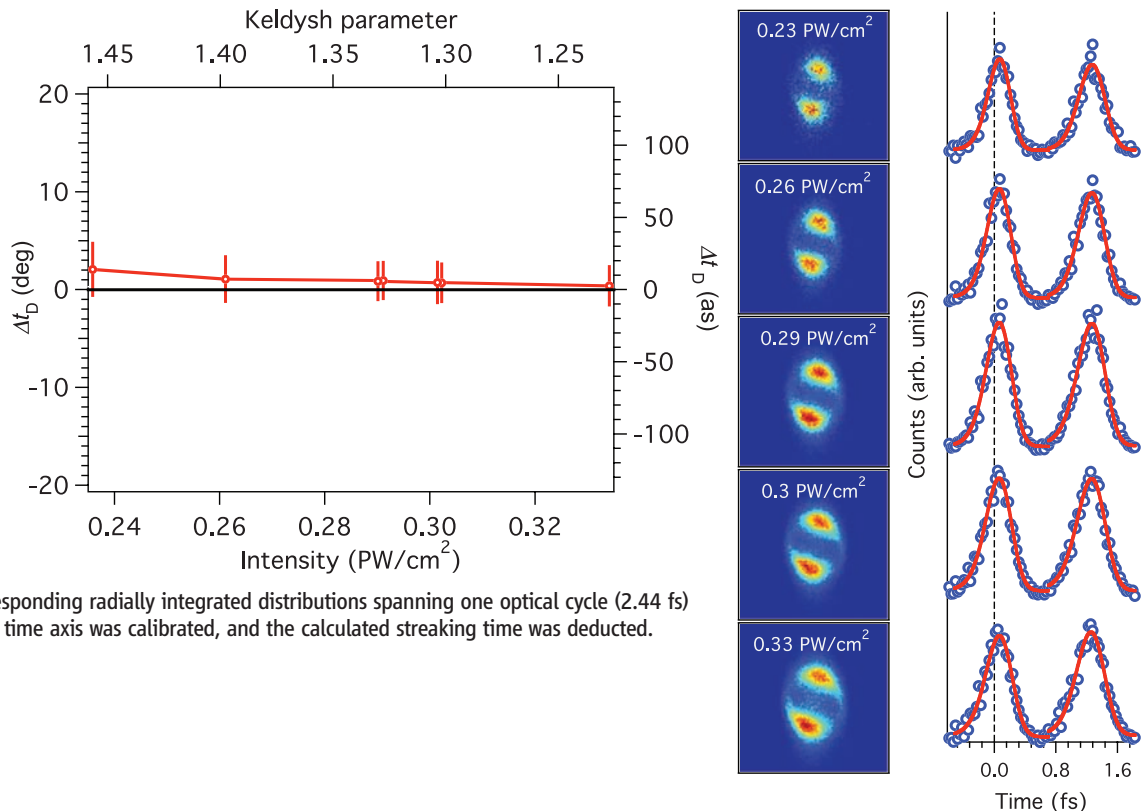
We conclude that with our measurement we can put an upper limit of 34 as on a Δt_D in the nonadiabatic tunneling regime with a γ ranging from 1.45 to 1.17. Quantum mechanical simulations using the time-dependent Schrödinger equation predict instantaneous ionization with no angular delay. We measured a weighted intensity-averaged tunneling delay time of 6.0 as with a standard deviation of the weighted mean of 5.6 as, which would result in an intensity-averaged upper limit of 12 as (21). Our experiments access a tunneling delay time in a conceptually well-defined manner that is closely related to the successful three-step model in high harmonic generation (8). We can clearly distinguish between the tunneling process and the consecutive acceleration of the free electron in the close-to-circular polarized laser field. This has given us direct experimental access to the tunneling delay time with a time accuracy of a few tens of attoseconds using attosecond angular streaking (17). The measured upper limit of the tunneling delay time is much shorter than the Buttiker-Landauer traversal time, Δt_T, which for the present conditions is predicted to range be-

tween 450 and 560 as. We reiterate that the Buttiker-Landauer traversal time, Δt_T, considers an entirely different aspect of the tunneling process. Our experimental results give a strong indication that there is no real tunneling delay time, and we expect that this conclusion will shed some light on the ongoing theoretical discussion on tunneling time.

References and Notes

1. L. A. MacColl, *Phys. Rev.* **40**, 621 (1932).
2. G. G. Paulus *et al.*, *Phys. Rev. Lett.* **80**, 484 (1998).
3. M. Uiberacker *et al.*, *Nature* **446**, 627 (2007).
4. R. Landauer, T. Martin, *Rev. Mod. Phys.* **66**, 217 (1994).
5. J. Ruseckas, *Phys. Rev. A* **63**, 052107 (2001).
6. H. G. Winful, *N. J. Phys.* **8**, 101 (2006).
7. J. G. Muga, R. S. Mayato, I. L. Egusquiza, in *Time in Quantum Mechanics*, J. G. Muga, R. S. Mayato, I. L. Egusquiza, Eds., vol. 734 of *Lecture Notes in Physics* (Springer, Berlin, ed. 2, 2008).
8. P. B. Corkum, *Phys. Rev. Lett.* **71**, 1994 (1993).
9. L. V. Keldysh, *Sov. Phys. JETP* **20**, 1307 (1965).
10. A. Zaïr *et al.*, *Phys. Rev. Lett.* **100**, 143902 (2008).
11. M. Meckel *et al.*, *Science* **320**, 1478 (2008).
12. G. L. Yudin, M. Y. Ivanov, *Phys. Rev. A* **63**, 033404 (2001).
13. M. Büttiker, R. Landauer, *Phys. Rev. Lett.* **49**, 1739 (1982).
14. M. Protopapas, C. H. Keitel, P. L. Knight, *Rep. Prog. Phys.* **60**, 389 (1997).
15. C. P. Hauri *et al.*, *Appl. Phys. B* **79**, 673 (2004).
16. J. Ullrich *et al.*, *Rep. Prog. Phys.* **66**, 1463 (2003).
17. P. Eckle *et al.*, *Nat. Phys.* **4**, 565 (2008).
18. H. R. Telle *et al.*, *Appl. Phys. B* **69**, 327 (1999).
19. D. J. Jones *et al.*, *Science* **288**, 635 (2000).
20. A. Apolonski *et al.*, *Phys. Rev. Lett.* **85**, 740 (2000).
21. Computational methods and error estimates are detailed on *Science* Online
22. M. V. Ammosov, N. B. Delone, V. P. Krainov, *Sov. Phys. JETP* **64**, 1191 (1986).
23. E. P. Wigner, *Phys. Rev.* **98**, 145 (1955).
24. A. Sommerfeld, *Phys. Z.* **8**, 841 (1907).
25. L. Brillouin, *Ann. Phys.* **349**, 203 (1914).
26. M. Büttiker, H. Thomas, *Ann. Phys.* **7**, 602 (1998).
27. This work was supported by Natural Center of Competence in Research Quantum Photonics (NCCR QP), research instrument of the Swiss National Science Foundation, the Alexander-von-Humboldt Stiftung, and the Deutsche Forschungsgemeinschaft. H.G.M. was supported by FOM (Fundamental Research on Matter), which is subsidized by NWO (Netherlands Organization for the Advancement of Research).

Optical Absorption and Radiative Thermal Conductivity of Silicate Perovskite to 125 Gigapascals

Hans Keppler,[1]* Leonid S. Dubrovinsky,[1] Olga Narygina,[1] Innokenty Kantor[1,2]

Mantle convection and plate tectonics are driven by the heat flow from Earth's core to the surface. The radiative contribution to heat transport is usually assumed to be negligible. Here, we report the near-infrared and optical absorption spectra of silicate perovskite, the main constituent of the lower mantle, to 125 gigapascals. Silicate perovskite remains quite transparent up to the pressures at the core-mantle boundary. Estimates of radiative thermal conductivity derived from these spectra approach 10 watts meter^{-1} kelvin^{-1} at lowermost mantle conditions, implying that heat conduction is dominated by radiation. However, the increase in radiative conductivity with temperature (T) is less pronounced than expected from a T^3 dependency.

Temperatures near Earth's core-mantle boundary are believed to be between 3300 and 4300 K (1). At these temperatures, one would expect heat transfer by radiation to be important because radiative thermal conductivity should increase with the third power of temperature (2–5). However, early experimental work appeared to imply that iron-bearing minerals generally become optically opaque already at moderately high pressures (6). Therefore, it has been thought that the minerals in Earth's lower mantle absorb radiation so strongly that the contribution of radiation to heat transport is negligible (1). Recently, the discovery of spin-pairing in

mantle minerals under high pressure (7) has led to a renewed interest in radiative conductivity, because spin-pairing could potentially change optical absorption spectra drastically and it may therefore have a strong effect on radiative heat transport (8, 9). At the same time, recent optical absorption measurements at high pressures suggested that iron-bearing mantle minerals do not necessarily become opaque at high pressures (10, 11). Rather, the changes in optical absorption with pressure strongly depend on the content and particularly on the oxidation state of iron in the sample. For example, ferropericlase, (Mg,Fe)O, synthesized at low pressures becomes optically opaque at high pressure because of its high Fe^{3+} content (9). However, samples annealed at 25 GPa have much lower concentrations of Fe^{3+} and remain optically transparent to deep lower mantle pressures (11). We therefore studied the optical absorption spectrum of aluminous silicate

perovskite, the main constituent of Earth's lower mantle, to 125 GPa, corresponding to the pressure near the core-mantle boundary. Perovskite is expected to be stable in the hot areas above the core-mantle boundary, which are the roots of mantle plumes, whereas it probably transforms to post-perovskite in cooler areas (1).

A sample of aluminous silicate perovskite with composition $(Mg_{0.892}Fe^{2+}_{0.059}Fe^{3+}_{0.042})$ $(Si_{0.972}Al_{0.028})O_3$ according to electron microprobe and Mößbauer data was synthesized from glass powder at 25 GPa and 2000°C in a multianvil press using a Re capsule. A doubly polished, optically clear piece of a crystal with 30-μm thickness was loaded into a modified Merrill Bassett diamond anvil cell. Pressure medium was neon; pressure was measured by ruby fluorescence. Near-infrared and optical absorption spectra were collected with use of a Bruker IFS 125 (Bruker Optics, Karlsruhe, Germany) Fourier transform spectrometer together with an all-reflecting microscope (12).

The measured absorption spectra from 1 bar to 125 GPa is shown in Fig. 1. The main feature seen is a broad band located between about 15,000 cm^{-1} and 20,000 cm^{-1}, depending on pressure. Position and width of this band are characteristic for a Fe^{2+}-Fe^{3+} intervalence charge transfer band; that is, light absorption is caused by the transfer of electrons from Fe^{2+} ions to neighboring Fe^{3+} ions (13, 14). The increasing absorption at high wave numbers is probably related to O^{2-}-Fe^{3+} ligand-to-metal charge transfer. The crystal field bands of Fe^{2+} are not visible in these spectra, although they can be found around 7000 cm^{-1} in the absorption spectrum of aluminum-free $(Mg,Fe)SiO_3$ perovskite (15). The invisibility of these bands is probably a combined result of their generally low intensity and the overlap with the intervalence charge transfer bands

[1]Bayerisches Geoinstitut, Universität Bayreuth, 95440 Bayreuth, Germany. [2]Advanced Photon Source, Argonne National Laboratory, Argonne, IL 60439, USA.

*To whom correspondence should be addressed. E-mail: hans.keppler@uni-bayreuth.de